Two-Dimensional Nonequilibrium Noncohesive and Cohesive Sediment Transport Model

M. C. Hung[1]; T. Y. Hsieh[2]; C. H. Wu[3]; and J. C. Yang, M.ASCE[4]

Abstract: The purpose of this paper is to develop an unsteady 2D depth-averaged model for nonuniform sediment transport in alluvial channels. In this model, the orthogonal curvilinear coordinate system is adopted; the transport mechanisms of cohesive and noncohesive sediment are both embedded; the suspended load and bed load are treated separately. In addition, the processes of hydraulic sorting, armoring, and bed consolidation are also included in the model. The implicit two-step split-operator approach is used to solve the flow governing equations and the coupling approach with iterative method are used to solve the mass-conservation equation of suspended sediment, mass-conservation equation of active-layer sediment, and global mass-conservation equation for bed sediment simultaneously. Three sets of data, including suspension transport, degradation and aggradation cases for noncohesive sediment, and aggradation, degradation, and consolidation cases for cohesive sediment, have been demonstrated to show the rationality and accuracy of the model. Finally, the model is applied to evaluate the desilting efficiency for Ah Gong Diann Reservoir located in Taiwan to show its applicability.

Introduction

Sediment transport determines the evolution of river bed in alluvial channels and affects both the functioning and the life span of many hydraulic structures. Hence, predictions of sediment transport in alluvial channels are important. In predicting the evolution process, the numerical models have become popular because of the low cost, flexibility in design for changing different plans, the ability to simulate riverbed deformation under large scale and long-term conditions, and it also provides a large quantity of information. Even though many three-dimensional (3D) numerical models for simulating sediment transport processes have been reported recently (Wu et al. 2000; Fang and Wang 2000; Li and Ma 2001), hydraulic engineers often adopt a 2D depth-averaged model in practice because of its efficiency and reasonable accuracy.

A number of 2D numerical models have been developed for computing bed deformation in alluvial channels. Most of these models were developed to solve a specific type of sediment prob-

lem. Celik and Rodi (1988) developed a model with Cartesian coordinates, but it is difficult to adequately handle complex boundaries in a natural channel. The Struiksma (1985) and the Shimizu and Itakura (1989) models ignored the local derivative term and are applicable only to steady flow conditions. Spasojevic and Holly (1990) and Kassem and Chaudhry (2002) proposed finite difference models to simulate the bed variations in a reservoir and channel bends, respectively. In the Spasojevic and Holly (1990) model, the advection, diffusion, and dispersion terms in the flow momentum equations were ignored and the transport mechanism of cohesive sediment was not embedded. In the Kassem and Chaudhry (2002) model, the sediment transport mechanism only considered the bed-load effect. Ziegler and Nisbet (1995) developed a model of cohesive sediment transport for reservoir sedimentation; however, the transport mechanism of noncohesive sediment was ignored. Thomas and McAnally (1985) presented a finite element model (TABS-2) to calculate the bed deformation in channels with cohesive and noncohesive sediment. In their model, the governing equations of sediment transport were solved in bed-material load concept, which may be improper for nonequilibrium sediment transport. The Rijn et al. (1990) model only considered suspended-load transport, so the model cannot solve the bed-load transport.

The purpose of this paper is to develop an unsteady 2D depth-averaged model for nonuniform sediment transport in alluvial channels. In this model, the orthogonal curvilinear coordinate system is adopted; the transport mechanisms of cohesive and noncohesive sediment are both embedded; the suspended load and bed load are treated separately. Moreover, hydraulic sorting, armoring, and bed consolidation are also included in the model. As for the numerical solution procedure, the implicit two-step split-operator approach (Hsieh and Yang 2004) is used to solve the flow governing equations, and the coupling approach with an iterative method are used to solve the mass-conservation equation of suspended sediment, mass-conservation equation of active-layer sediment, and global mass-conservation equation for bed sediment simultaneously. Three sets of data, including suspension

[1]Ph.D. Candidate, Dept. of Civil Engineering, National Chiao Tung Univ., 1001 Ta Hsueh Rd., Hsinchu, Taiwan 30050, R.O.C. E-mail: mchung.cv87g@nctu.edu.tw

[2]Researcher, Energy and Environment Laboratories, Industrial Technology Research Institute, Bldg. 24, Section 4, Chung Hsing Rd., Chutung, Hsinchu, Taiwan 310, R.O.C. E-mail: hsieh0182@itri.org.tw

[3]Adjunct Researcher, Water Resources Agency, Institute of Planning and Hydraulic Research, 1340 Chung-Cheng Rd., Wu-Fong, Taichung, Taiwan, R.O.C. E-mail: wcs@wrap.gov.tw

[4]Professor, Dept. of Civil Engineering and Hazard Mitigation Research Center, National Chiao Tung Univ., 1001 Ta Hsueh Rd, Hsinchu, Taiwan 30050, R.O.C. E-mail: jcyang@mail.nctu.edu.tw

transport, degradation, and aggradation cases for noncohesive sediment, and degradation, aggradation, and consolidation cases for cohesive sediment, have been demonstrated to show the rationality and accuracy of the model. Finally, the model is applied to the Ah Gong Diann Reservoir located in Taiwan to demonstrate its applicability.

Description of Model

Governing Equations

Flow Equations

The 2D depth-averaged flow equations in orthogonal curvilinear coordinate can be written as follows (Hsieh and Yang 2003): Continuity equation

$$h_1 h_2 \frac{\partial d}{\partial t} + \frac{\partial}{\partial \xi}(h_2 \bar{\bar{u}} d) + \frac{\partial}{\partial \eta}(h_1 \bar{\bar{v}} d) = 0 \tag{1}$$

Momentum equations

$$\frac{\partial \bar{\bar{u}}}{\partial t} + \frac{\bar{\bar{u}}}{h_1}\frac{\partial \bar{\bar{u}}}{\partial \xi} + \frac{\bar{\bar{v}}}{h_2}\frac{\partial \bar{\bar{u}}}{\partial \eta} + \frac{1}{h_1 h_2}\frac{\partial h_1}{\partial \eta}\bar{\bar{u}}\bar{\bar{v}} - \frac{1}{h_1 h_2}\frac{\partial h_2}{\partial \xi}\bar{\bar{v}}^2$$

$$= -\frac{g}{h_1}\frac{\partial}{\partial \xi}(z_b + d) + \frac{1}{\rho h_1 h_2 d}\left[\frac{\partial}{\partial \xi}(h_2 T_{11}) + \frac{\partial}{\partial \eta}(h_1 T_{12}) + \frac{\partial h_1}{\partial \eta}T_{12}\right.$$

$$\left. - \frac{\partial h_2}{\partial \xi}T_{22}\right] - \frac{\tau_{b_1}}{\rho d} + \frac{1}{\rho h_1 h_2 d}\left[-(h_2 \tau_{11})_s\frac{\partial z_s}{\partial \xi} + (h_2 \tau_{11})_b\frac{\partial z_b}{\partial \xi}\right.$$

$$\left. - (h_1 \tau_{12})_s\frac{\partial z_s}{\partial \eta} + (h_1 \tau_{12})_b\frac{\partial z_b}{\partial \eta}\right] \tag{2}$$

$$\frac{\partial \bar{\bar{v}}}{\partial t} + \frac{\bar{\bar{u}}}{h_1}\frac{\partial \bar{\bar{v}}}{\partial \xi} + \frac{\bar{\bar{v}}}{h_2}\frac{\partial \bar{\bar{v}}}{\partial \eta} + \frac{1}{h_1 h_2}\frac{\partial h_2}{\partial \xi}\bar{\bar{u}}\bar{\bar{v}} - \frac{1}{h_1 h_2}\frac{\partial h_1}{\partial \eta}\bar{\bar{u}}^2$$

$$= -\frac{g}{h_2}\frac{\partial}{\partial \eta}(z_b + d) + \frac{1}{\rho h_1 h_2 d}\left[\frac{\partial}{\partial \xi}(h_2 T_{12}) + \frac{\partial}{\partial \eta}(h_1 T_{22}) - \frac{\partial h_1}{\partial \eta}T_{11}\right.$$

$$\left. + \frac{\partial h_2}{\partial \xi}T_{12}\right] - \frac{\tau_{b_2}}{\rho d} + \frac{1}{\rho h_1 h_2 d}\left[-(h_2 \tau_{12})_s\frac{\partial z_s}{\partial \xi} + (h_2 \tau_{12})_b\frac{\partial z_b}{\partial \xi}\right.$$

$$\left. - (h_1 \tau_{22})_s\frac{\partial z_s}{\partial \eta} + (h_1 \tau_{22})_b\frac{\partial z_b}{\partial \eta}\right] \tag{3}$$

in which ξ and η=orthogonal curvilinear coordinates in streamwise axis and transverse axis, respectively; h_1 and h_2=metric coefficients in ξ and η directions, respectively ($h_1=h_2=1$ for straight channels; $h_1=1$ and $h_2=1/r$ for cylindrical flow; r =radius of curvature); u and v=velocity velocity components in ξ and η directions, respectively; ρ=fluid density; g=gravitational acceleration; t=time; d=depth; z_b=bed elevation; z_s=water surface elevation; double overbar $\bar{(}$=depth average; subscripts s and b indicate the dependent variables at the water surface and channel bed, respectively; and T_{11}, T_{12}, T_{22}=effective stresses. The present model ignores the dispersion stresses and uses the Boussinesq eddy-viscosity concept to simulate laminar viscous stresses and turbulent stresses, as described in details by Hsieh and Yang (2003). $\tau_{b1}=C_f\rho\bar{\bar{u}}(\bar{\bar{u}}^2+\bar{\bar{v}}^2)^{1/2}$ and $\tau_{b2}=C_f\rho\bar{\bar{v}}(\bar{\bar{u}}^2+\bar{\bar{v}}^2)^{1/2}$ (Rastogi and Rodi 1978) are the shear stresses at the channel bottom in the ξ and η directions, respectively; $C_f=g/c^2$=friction factor; and c =Chezy factor.

Sediment Transport Equations

The 2D depth-averaged sediment transport equations in orthogonal curvilinear coordinate can be written as follows (Spasojevic and Holly 1990): Mass-conservation equation of suspended sediment

$$\frac{\partial \bar{\bar{C}}_k}{\partial t} + \frac{\bar{\bar{u}}}{h_1}\frac{\partial \bar{\bar{C}}_k}{\partial \xi} + \frac{\bar{\bar{v}}}{h_2}\frac{\partial \bar{\bar{C}}_k}{\partial \eta}$$

$$= \frac{1}{h_1 h_2 d}\frac{\partial}{\partial \xi}[h_2 (Q_1)_k d] + \frac{1}{h_1 h_2 d}\frac{\partial}{\partial \eta}[h_1 (Q_2)_k d] + \frac{S_k}{\rho d} \tag{4}$$

Mass-conservation equation of active-layer sediment

$$\rho_s(1-p)h_1 h_2\frac{\partial(\beta_k E_m)}{\partial t} + \frac{\partial}{\partial \xi}[h_2 (q_{b1})_k] + \frac{\partial}{\partial \eta}[h_1 (q_{b2})_k] + S_k - (S_f)_k$$

$$= 0 \tag{5}$$

Global mass-conservation equation for bed sediment

$$\rho_s(1-p)h_1 h_2\frac{\partial z_b}{\partial t} + \sum\left[\frac{\partial}{\partial \xi}(h_2 (q_{b_1})_k) + \frac{\partial}{\partial \eta}(h_1 (q_{b_2})_k) + S_k\right] = 0 \tag{6}$$

where c=concentration; ρ_s=density of sediment; β=active-layer size fraction; p=porosity of the bed material; E_m=active-layer thickness; q_{b_1}, q_{b_2}=components of bed-load flux in the ξ and η directions, respectively; s=suspended-sediment source; S_f =active-layer floor source; Q_1, Q_2=suspended-sediment flux due to both turbulent diffusion and lateral dispersion in the ξ and η directions, respectively; and subscript k indicates the kth size class.

The bed-load flux of cohesive sediment [sediment particle size less than 0.062 mm (Lane et al. 1974)] can be regarded as zero. The net bed-load flux of noncohesive sediment adopted in this study is presented herein as

$$(q_{b_i})_k = \zeta_k\beta_k q_{b_i}^t \tag{7}$$

For example, bed-load flux in the ξ direction for the kth size class can be expressed as (Van Rijn 1984a)

$$(q_{b_\xi})_k = \zeta_k\beta_k\left(0.053\rho_s\sqrt{(s-1)gD_k}D_k\frac{T_k^{2.1}}{D_{*k}^{0.3}}\right) \tag{8}$$

where $q_{b_i}^t$=theoretical bed-load transport capacity in the i (ξ or η) direction; $s=\rho_s/\rho$=dimensionless sediment density; D=sediment diameter; $D_{*k}=D_k\{[(s-1)g]/v^2\}^{1/3}$=dimensionless particle diameter; $T_k=[u_*^2-(u_{*c})_k^2]/[(u_{*c})_k^2]$=transport-stage parameter; u_* $=(u\sqrt{g})/(c_1)$=effective bed-shear velocity; c_1 $=18\log[(12d)/(3D_{90})]$=grain Chezy coefficient; u_{*c}=critical shear velocity evaluated from Shields diagram. This load is adjusted by ζ, a so-called hiding factor. In this study, the Karim et al. (1987) empirical relation, $\zeta_k=(D_k/D_{50})^{0.85}$, is adopted where D_{50}=median sediment-particle size. The adjusted load is modified by β to reflect the availability of the particular size class in the active-layer elemental volume.

According to Van Rijn (1984b) and Holly and Rahuel (1990), the suspended-sediment source is the combination of deposition and resuspension and can be expressed as

$$S_k = (S_e)_k - (S_d)_k \tag{9}$$

where S_e=entrainment component; and S_d=deposition component.

For noncohesive sediment, entrainment and deposition component can be calculated by

$$(S_e)_k = \rho(w_l)_k \beta_k (C_e)_k \qquad (10a)$$

$$(S_d)_k = \rho(w_f)_k (C_d)_k \qquad (10b)$$

where w_l=lift-off velocity (Hu and Hui 1996); C_e=entrainment near-bed concentration; w_f=noncohesive sediment fall velocity (Van Rijn 1984b); and C_d=near-bed deposition concentration.

The entrainment near-bed concentration (C_e) is evaluated using the van Rijn (1984b) expression

$$(C_e)_k = 0.015 \frac{D_k}{a} \frac{T_k^{1.5}}{D_{*k}^{0.3}} \qquad (11)$$

where a=relative height above the bed.

An empirical relation proposed by Lin (1984) is used to evaluate the near-bed deposition concentration $(C_d)_k$

$$C_{d_k} = \left[3.25 + 0.55 \ln\left(\frac{w_{fk}}{\kappa u_*} \right) \right] \bar{\bar{C}}_k \qquad (12)$$

For cohesive sediment, S_d is given by the Krone (1962) formulation

$$(S_d)_k = \left(1 - \frac{\tau_b}{\tau_{cd}} \right)(w_f)_k \bar{\bar{C}}_k \quad \text{for } \tau_b < \tau_{cd} \qquad (13a)$$

$$(S_d)_k = 0 \quad \text{for } \tau_b \geqslant \tau_{cd} \qquad (13b)$$

where τ_{cd}=critical shear stress for deposition; $w_f = F w_s$ =cohesive sediment fall velocity; w_s=particle settling velocity following the Stokes law; F=flocculation factor$= C_F D_k^{-1.8}$ (Teisson 1991); C_F=coefficient [the value of 250 was adopted in the Teisson (1991) paper].

The present model recognizes two modes of S_e of cohesive beds: particle erosion S_{ep} and mass erosion S_{em}. The following equations are used for the particle and mass erosion, respectively (Partheniades 1965; Ariathurai 1974):

$$(S_{ep})_k = \beta_k M \left(\frac{\tau_b}{\tau_{cep}} - 1 \right) \quad \text{for } \tau_b > \tau_{cep} \qquad (14a)$$

$$(S_{em})_k = \frac{\rho_d F_d}{d \Delta t} \quad \text{for } \tau_b > \tau_{cem} \qquad (14b)$$

$$(S_e)_k = (S_{ep})_k + (S_{em})_k \qquad (14c)$$

where $M = 0.55(C_k/1,000)^3$ (Teisson 1991) =material coefficient; τ_{cep}=critical shear stress for particle erosion; τ_{cem}=critical bed shear stress for mass erosion; ρ_d=bulk density (Ariathurai 1974); F_d=characteristic depth of erosion, which can be substituted by E_m; Δt=time step; and S_e=total entrainment component of cohesive sediment.

According to the concept of Bennett and Nordin (1977), the active-layer thickness during erosion is the following:

$$E_m = -20(z_b^{n+1} - z_b^n) \qquad (15)$$

where the superscript $n+1$=variable at time level $(n+1)\Delta t$; and the superscript n=variable at time level n.

As the bed surface approaches the armored condition, then Eq. (15) leads to a zero active-layer thickness. In such situations, the Borah et al. (1982) armored-layer thickness can be used as a limiting value for the active-layer thickness

$$E_m = -20(z_b^{n+1} - z_b^n) + \frac{1}{\sum_{k=m}^{K} \beta_k} \frac{D_m}{1-p} \qquad (16)$$

where D_m=smallest nonmoving size class.

The active-layer floor elevation is assumed to remain constant during deposition; hence, S_f can be regarded as zero and the active-layer thickness can be defined as

$$E_m^{n+1} = E_m^n + (z_b^{n+1} - z_b^n) \qquad (17)$$

Movement of the active-layer floor ($z_b - E_m$) generates the active-layer floor source S_f. If the active-layer floor descends during erosion, then S_f has the form (Spasojevic and Holly 1990).

$$S_f = -\rho_s(1-p) \frac{\partial}{\partial t} [(\beta_s)_k (Z_b - E_m)] \qquad (18)$$

where $(\beta_s)_k$=kth size-class fractional representation in the active stratum.

Q_1 and Q_2 appearing in Eq. (4) can be represented by a simple gradient transport model (Almquist and Holley 1985; Hsieh and Yang 2005)

$$(Q_1)_k = \varepsilon_\xi \frac{\partial \bar{\bar{C}}_k}{\partial \xi} \quad (Q_2) = (\varepsilon_\eta + e_\eta) \frac{\partial \bar{\bar{C}}_k}{\partial \eta} \qquad (19)$$

where ε_ξ=turbulent diffusion coefficient in ξ direction$=5.93 U_* d$ (Elder 1959); ε_η=turbulent diffusion coefficient in η direction $=0.23 U_* d$ (Elder 1959); e_η=lateral dispersion coefficient $=25[(\bar{\bar{u}}d)/(U_* r)]^2$ (Fischer et al. 1979); and U_*=shear velocity.

Sorting, Armoring, and Consolidation for Bed Material

Most river beds consist of grains with a broad size fraction. If the flow over such a bed is depleted of sediment, fine particles are entrained more easily and the bed surface will become progressively coarser. Ultimately, an armor coat of large particles may form, and that stops further degradation. During the aggradation process, the bed surface will be progressively finer. Updating the bed composition at every time step is necessary and crucial to a sediment routing model. In the present study, the model adopts the conventional sorting and armoring techniques, which were proposed by Bennet and Nordin (1977). In the model, the river bed can be divided into several layers, and bed composition counting is accomplished through the use of two or three armor layers, depending on whether scouring or deposition occurs during the time step.

Modeling morphological changes of a cohesive bed, the degree of consolidation of the bed must be specified since it controls the bed level variation and the initiation and rate of erosion. As mentioned before, the present model divides the bed into a number of layers; therefore, the different critical shear stresses for erosion can be specified in each layer to reflect the consolidation effect for cohesive sediment. The consolidation level of mud deposits can be counted based upon experiences of Migniot (1989). Besides, when deposition occurs, the deposit always goes into the first layer, the thickness of which increases consequently, and the τ_{cep} and τ_{cem} for the new-deposit sediment are set as 0.064 N/m^2 and 0.143 N/m^2 (Teisson 1991).

Numerical Methodology

The implicit two-step split-operator approach proposed by Hsieh and Yang (2004) is used herein for flow computation. The first step (dispersion step) is to compute the provisional velocity in the

momentum equation without considering the pressure gradient and bed friction. The second step (propagation step) is to correct the provisional velocity by considering the effect of the pressure gradient and bed friction.

The dispersion step includes convection and diffusion terms. In order to catch the flow direction, a simple hybrid scheme is used for the convection terms. Diffusion terms are discretized using the concept of control volume. Coupling with the convection and diffusion terms, the alternating direct implicit (ADI) scheme is adopted to solve the discretization equations. The propagation step includes pressure, gravity, and bottom shear stresses terms, and none of the velocity gradient appears in this step. The propagation step can be discretized into a simple algebraic equation while the unknown can be solved directly. Similar to diffusion terms, the continuity equation can be discretized by using the concept of control volume and solved by the ADI scheme. The detailed computation methodologies can be referred to in Hsieh and Yang (2004).

The primary sediment variables are interrelated to each other through the auxiliary relations. For example, S appears simultaneously in all of the sediment equations; therefore, the perturbation of $\bar{\bar{C}}$ affects the computed results of β and z_b. In addition, z_b and β may be affected by the change of bed-load flux in each computation time step. It is obvious that from the arguments mentioned above, a coupling approach has to be used to solve the system equations of sediment.

The mass-conservation equation of suspended sediment is split into two successive steps: advection step and diffusion step. The advection step contains advection and source terms. In order to obtain the better accuracy of solution for the advection part, a characteristics approach is used herein. The diffusion step contains diffusion terms, which will be discretized by using the concept of control volume. Similarly, in sediment transport processes, Eqs. (5) and (6) are discretized by the control-volume concept.

Boundary Conditions

Three types of boundary, namely, inlet, outlet, and solid walls are considered. Discharge hydrograph per unit width, concentration distribution, bed elevation, and active-layer size fraction can be specified along the inlet section. Water surface elevation, $\partial\bar{\bar{C}}/\partial\xi=0$, $\partial z_b/\partial\xi=0$, and $\partial\beta/\partial\xi=0$ can be specified along the outlet section. At the solid boundaries, the law of the wall is applied outside the viscous sublayer and transition layer, in the range of $30<y^+<100$, in which $y^+=y_w u_*/\upsilon$, and $y_w=$distance between the first computational grid point adjacent to the wall and the wall itself. Within the wall region, the universal law of the wall is applied as

$$u^+ = \frac{1}{k}\ln(Ey^+) \qquad (20)$$

where $u^+=u_w/u_*$; $u_w=$depth-averaged velocity near the wall; and $E=$roughness parameter$=9$. On the basis of law of the wall, a so-called wall function (Rastogi and Rodi 1978) is formulated, which links the near-wall velocities. Using the logarithmic velocity law given by Eq. (20) and the expression for wall shear stress, τ_w can be expressed as (Biglari and Sturm 1998)

$$\frac{\tau_w}{\rho} = \frac{ku_* u_w}{\ln(Ey^+)} \qquad (21)$$

The above wall shear stress is used as the wall boundary condition and is substituted into the momentum equation in the wall region to solve for the velocity component parallel to the wall. Besides, $\partial\bar{\bar{C}}/\partial\eta=0$, $\partial z_b/\partial\eta=0$, and $\partial\beta/\partial\eta=0$ are specified in the solid wall.

Overall Solution Procedure

The overall solution procedures for solving flow and sediment equations can be listed as follows:
1. Calculate the provisional velocities from the momentum Eqs. (2) and (3) without the pressure gradient terms to complete the dispersion step.
2. Compute Eq. (1) implicitly to obtain depth increment by the ADI method.
3. The unknown velocities are calculated by correcting the provisional velocities with the pressure gradient and bed friction to complete the propagation step.
4. Steps 1–3 are required to compute repeatedly until successive predictions of velocities and depth increment no longer change along the flow domain.
5. Solve the system of equations including Eqs. (5) and (6), and advection step of mass-conservation equation of suspended sediment simultaneously by Newton-Raphson scheme to obtain the provisional $\bar{\bar{C}}$, β, and z_b.
6. Solve the diffusion step of mass-conservation equation of suspended sediment by the ADI method.
7. Repeat Steps 5–6 until the change of $\bar{\bar{C}}$, β, and z_b between predictor and corrector satisfies the convergence criterion.
8. Return to Step 1 and proceed to the next time step.
9. Repeat the above procedures until a steady state solution is reached (for steady state flows) or the specific time period is completed (for unsteady flows).

Model Verifications

In order to show the capability of the proposed model, three sets of data, including suspension transport, degradation, and aggradation cases for noncohesive sediment, and aggradation, degradation, and consolidation cases for cohesive sediment, have been demonstrated to verify the accuracy of the model. In all cases, the grid systems are designed to be fine enough to meet the requirement of adequate resolution.

Suspension Transport Case

If the suspended-sediment source term (S) is ignored in the mass-conservation equation of suspended sediment [Eq. (4)], the remaining equation is identical to the contaminant transport equation. Hence, the experimental data for contaminant transport conducted by Almquist and Holley (1985) are adopted to validate the suspension transport mechanism embedded in the present model.

In Almquist and Holley's experiment, as shown in Fig. 1, the channel was rectangular with smooth bed and consisted of 2.5 bends in alternating directions interconnected by straight reaches. The central angle of the full bends was 125°; that of the half-bend, which served as a flow developing section, was 62.5°. The centerline radius of curvature was 4.95 m, the channel width was 1.65 m, the length of the straight tangent sections was 2.48 m, the channel slope was 0.001, and Manning's roughness was 0.015. The discharge given from the upstream end of the channel was 0.099 m³/s, the average velocity was about 0.49 m/s, and the average flow depth was 0.12 m. The flow tracer was a
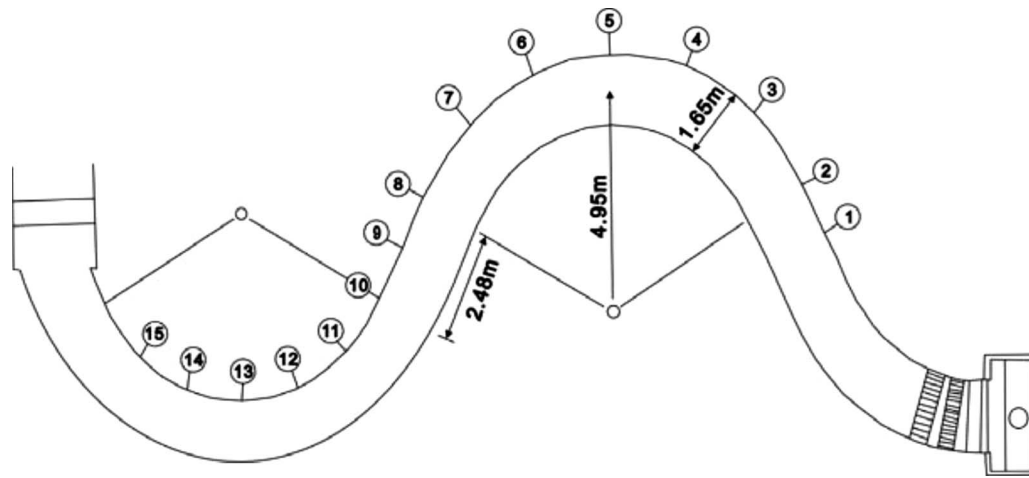
Fig. 1. Channel geometry and measured stations of suspension transport case [adapted from Almquist and Holley (1985)]

60,000 mg/1 mixing solution of salt and methanol in which the density was adjusted to match the water density. Tracer injections were made at two locations, 0.08 m from the left and right banks of station 2 shown in Fig. 1.

The mesh of 105×21 was used in the simulation. The upstream boundary condition was the inflow discharge per unit width, the downstream boundary condition was the measured water-surface elevation, and no-slip boundary was used at the banks. The tracer concentration was specified at the injected location.

Fig. 2 shows the variation of velocity ratio U/UM across the dimensionless channel width Y/B obtained from simulated results and the measured data, where U=depth-averaged longitudinal velocity; UM is cross-section averaged longitudinal velocity; and Y/B represents the dimensionless lateral position (B=channel width), where 0 is at the centerline, −0.5 is at the left bank, and 0.5 is at the right bank. One can observe from Fig. 2 that the simulated results have fairly good agreement with measured data. The velocity-distribution behavior is similar for the two bends in which one is from stations 2 to 8 and the other is from stations 10 to 15. In the entrance of the bend, the maximum velocities occur near the inner bank. As the flow moves farther downstream, the velocity distribution then begins to flatten out. The longitudinal velocity near the outer bank increases along the bend and the maximum velocity then shifts toward the opposite bank.

As pointed out by Almquist and Holley (1985), Elder (1959), and Fischer et al. (1979), formulas embedded in the present model were not suitable for the present case. Hence, by adjusting ε_ξ and ε_η, which were assumed to be spatially variable along the channel, these two parameters can be calibrated by comparing measured and simulated concentrations in the case for injection near the left bank of station 2. By using the calibrated parameters, the accuracy of the suspension transport model was quantitatively assessed by comparing measured and simulated concentrations in the case for injection near the right bank of station 2. Fig. 3 shows the variation of concentration ratio C/C_{max} across the lateral position obtained from simulated results and the measured data in the case for injection near the right bank of station 2, where C =depth-averaged concentration; and C_{max}=maximum depth-averaged concentration measured at that station and this value would decrease along the channel. From Fig. 3, one can find that model results consistently agree with measurements along the channel. The concentration peak keeps at the right bank in each

station. The lateral transport effect causes the tracer to move toward the left bank and the concentration distribution across the section approaches uniform gradually. In summary, from the above analyses, it is reasonable to positively conclude the model capability for the wash load transport process.
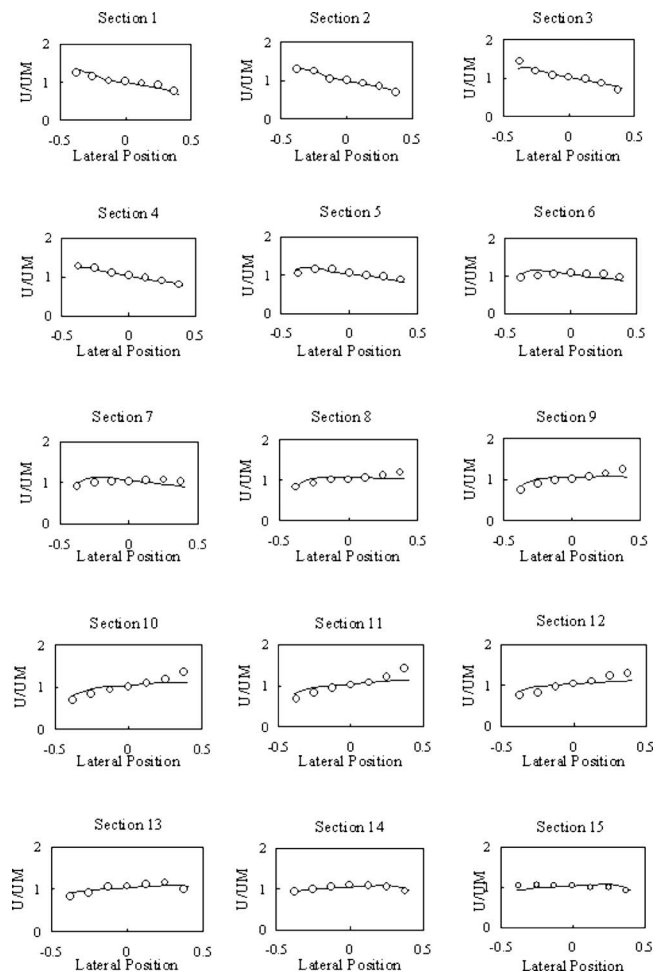

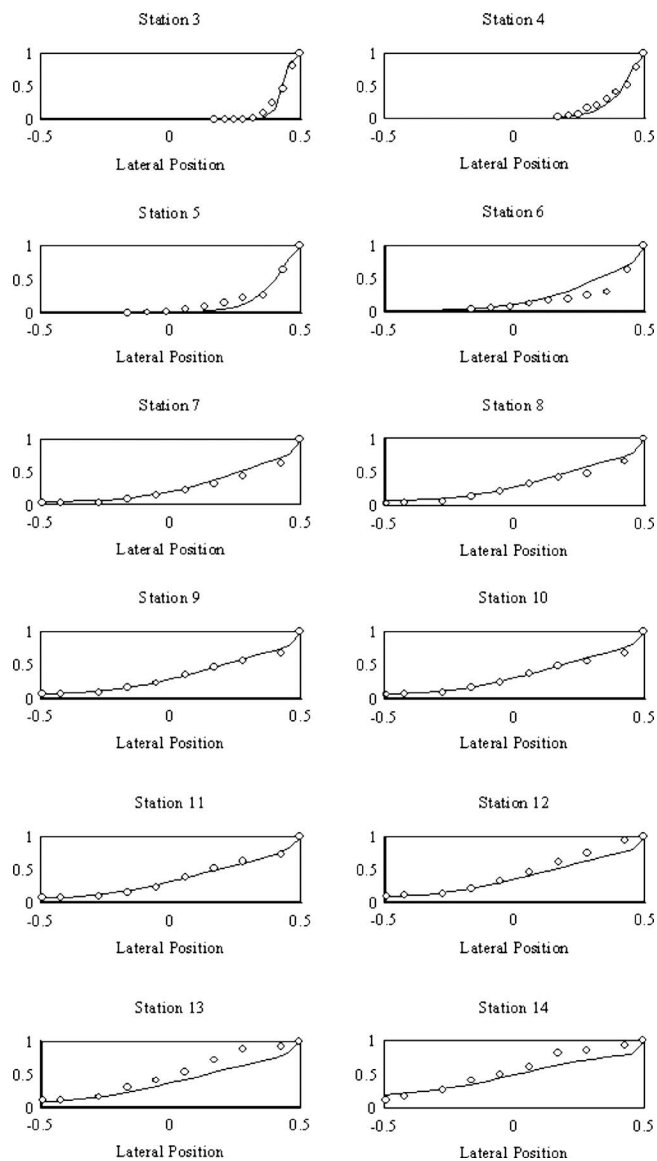**Fig. 2.** Lateral distribution of velocity ratio U/UM for Almquist and Holley's simulation

Fig. 3. Lateral distribution of depth-averaged concentration ratio C/C_{max} for Almquist and Holley's simulation

Fig. 4. Size gradation curve of Suryanarayana's experiment

Degradation and Aggradation Cases for Noncohesive Sediment

The mechanism of degradation and aggradation for noncohesive sediment embedded in the present model are validated by comparing the simulated results with experimental data obtained by Suryanarayana (1969).

A straight flume having a rectangular cross section 18.3 m long and 0.6 m wide was used in Suryanarayana's experiment. In the degradation case, the clean water with unit discharge 0.068 m^2/s was specified at the channel inlet; the water-surface elevation varied from 0.292 m to 0.302 m at the channel outlet. The particle gradation for the bed material and the sediment inflow are shown in Fig. 4 and denoted as sand 3 and sand 2, respectively. In the aggradation case, the unit discharge and sediment concentration of uniform sand (sand 2 of Fig. 4, representative diam is 0.45 mm) given at the upstream end of the channel were 0.024 m^2/s and 409 ppm, respectively. The water-surface elevation at the downstream end of the channel was 0.257 m.

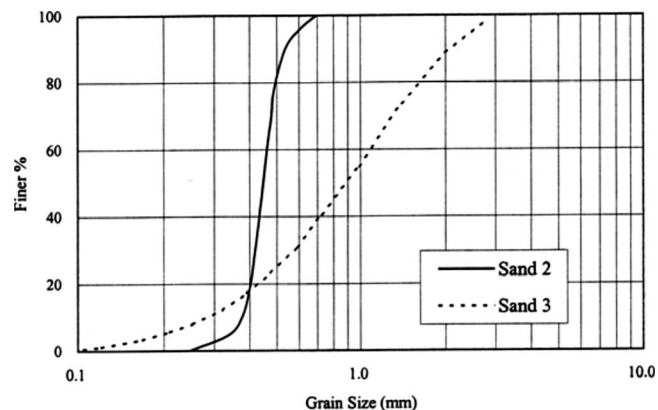The uniform mesh of 51×5 was used in the simulation. The upstream boundary conditions were the inflow discharge per unit width and the sediment concentration. The measured water-surface elevation and the no-slip condition were used for the downstream end and the channel banks, respectively.

Fig. 5 shows the bed and water surface profile during degradation processes obtained from simulated results and measured data at $t = 2.25$ h, 7 h, and 13 h. By comparing the simulated and measured results in Fig. 5, it is evident that the simulated results have much less deviation from the measured data. From Fig. 5, one can also observe that water depth increases while bed slope decreases as degradation progressed. Bed degradation occurs mainly near upstream inlet at $t = 2.25$ h. As time increases, the process of bed degradation continuously progresses and passes on to the downstream; at $t = 13$ h, the degradation can be observed in the whole channel.

Fig. 6 shows the bed and water-surface profile during aggradation processes obtained from simulated results and measured data. In Fig. 6, the convincing agreement between the simulated results and measured data is observed. The excess sediment is deposited near the entrance of the stream because the sediment supply is grater than the transport capacity of the stream. The bed rises and the water depth and the slope of the bed increase, so that, to satisfy the updated hydraulic conditions, a new equilibrium slope will be established. Meanwhile, a discontinuity of the bed can be observed with new equilibrium slope and can be called as aggrading front (Suryanarayana 1969). Afterward, sediment enters the downstream of the aggrading front, the hydraulic conditions are not favorable enough for the sediment transported downstream, and, therefore, is deposited in this reach. Since there is a discontinuity near the aggrading front, the backwater effect is created and some part of the sediment would be deposited upstream of the aggrading front. Thus, the deposition of sediment may proceed both upstream and downstream of the aggrading front. Finally, at $t = 10$ h, another new equilibrium slope is built over the whole stream and the stream can be considered as stable; no deposition or scouring occurs. Nevertheless, since the hybrid scheme adopted by the present study has only the first-order accuracy, the deviations between simulated results and measured data are larger near the shock front, as indicated in Fig. 6.

The studies demonstrated above show the capability of the present model to tackle the degradation and aggradation processes for noncohesive sediment. In order to further examine the transport mechanism of cohesive sediment embedded in the present
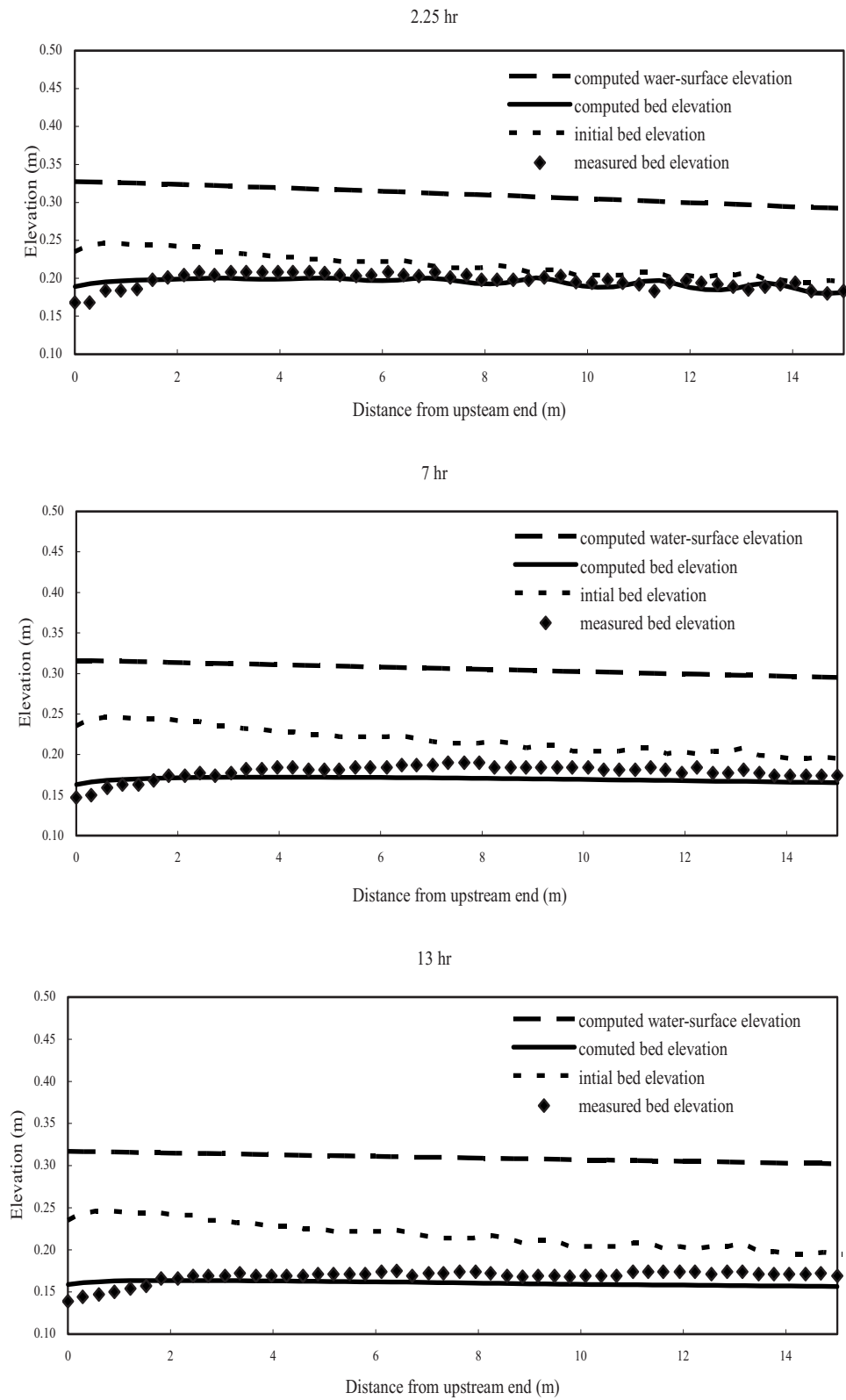
2.25 hr

7 hr

13 hr

Fig. 5. Variation of longitudinal bed profile with time (degradation case)
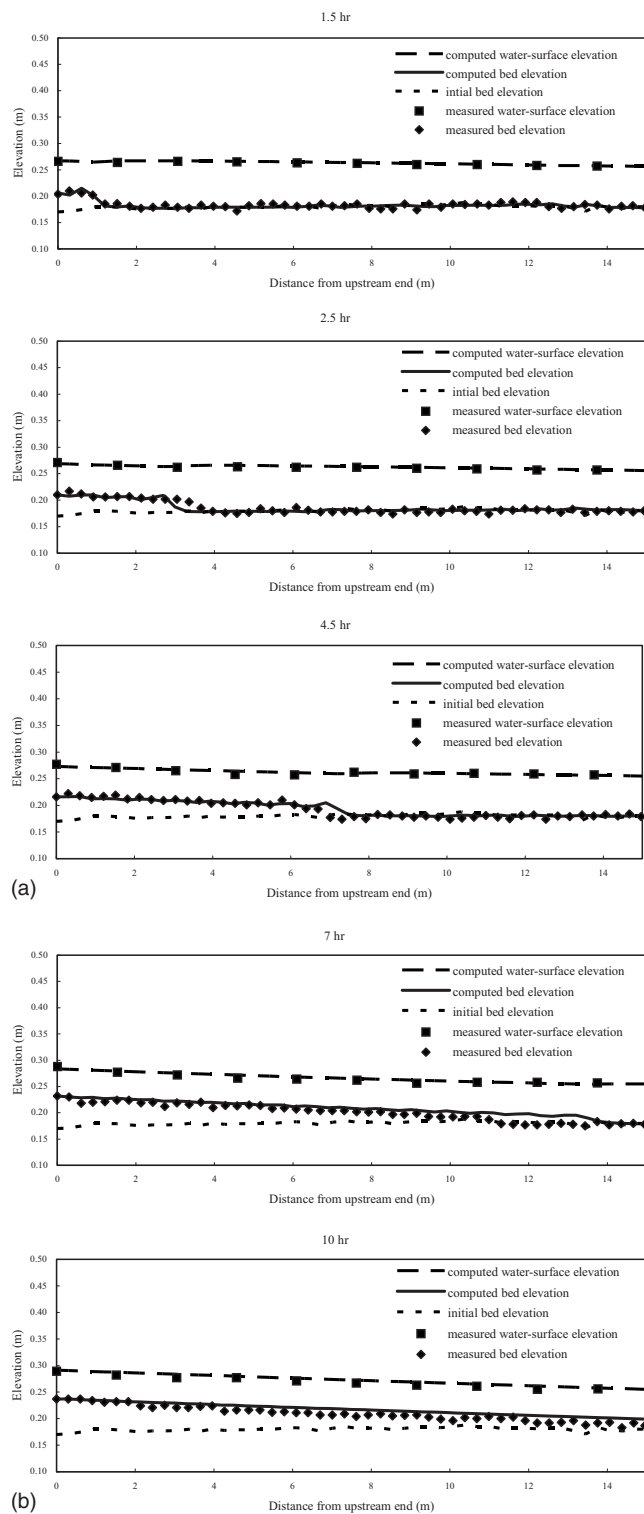
Fig. 6. Variation of longitudinal bed profile with time (aggradation case)

model, a set of cohesive sediment cases is studied in the following paragraphs.

Degradation, Aggradation, and Consolidation Test for Cohesive Sediment

Due to lack of available experimental data for cohesive sediment in the literature, hereafter, a few specific hypothetical test cases are used to demonstrate the model's capability.

Table 1. Cohesive Sediment Data for Aggradation Simulation

Set number	Case number	Inflow discharge (cms)	τ_{cd} (N/m^2)	Inflow concentration (ppm)
1	1	2	0.06	2,000
	2	8		
	3	16		
	4	24		
2	1	24	0.06	2,000
	2		0.10	
	3		0.40	
	4		1.10	
3	1	24	0.06	2,000
	2			4,000
	3			6,000
	4			10,000

Aggradation Process

The cases with straight rectangular channel by changing different inflow discharge, critical shear stress for deposition τ_{cd}, and inflow concentration were studied. The channel has a length of 8,000 m, a width of 100 m, a slope of 0.0005, and Manning's roughness of 0.03. The sediment data with three size classes: 0.001 mm (clay, 33.33%), 0.01 mm (33.33%), and 0.05 mm (silt, 33.33%) were chosen for this study. In each case, the water-surface elevation for the outlet of channel was fixed at 4.5 m, the zero initial concentration was used, the total simulation time was 6 days, and the mesh 81×11 was used in the simulation.

Three sets of scenarios with four various inflow discharge τ_{cd} and inflow concentration, were designed and shown in Table 1.

The results of maximum aggrading height H_m and aggrading outset location L_o, which is equal to the distance from the upstream end to the location of aggrading outset, obtained from the model are given in Table 2. For set 1, one can deduce that the bed shear stress τ_b may increase as inflow discharge increases and the chance for $\tau_b < \tau_{cd}$ correspondingly decreases. Thus, one can observe from Table 2 that H_m decreases and L_o increases. This consequence indicates that the aggrading outset location moves downstream, from case 1 to case 4 of set 1. Similarly, the increase of τ_{cd} may raise the probability of deposition; So, for set 2, H_m increases gradually and the aggrading outset location moves upstream from case 1 to case 4 as shown in Table 2. The cases in set 3 only change the inflow concentration, in which the same flow condition and deposition criteria are considered. Hence, L_o keeps the same in each case and H_m increases due to the increase of inflow concentration from case 1 to case 4 of set 3, as shown in Table 2.

Degradation Process

The simulated conditions, including the geometry of channel, sediment data, water-surface elevation at the outlet of channel,

**Table 2.** Results of H_m and L_o for Aggradation Cases of Cohesive Sediment

	Set 1		Set 2		Set 3	
Case	H_m (m)	L_o (m)	H_m (m)	L_o (m)	H_m (m)	L_o (m)
1	0.00087	0	0.00074	1,600	0.00074	1,600
2	0.00081	0	0.00078	1,000	0.00147	1,600
3	0.00077	800	0.00085	0	0.00220	1,600
4	0.00074	1,600	0.00088	0	0.00368	1,600

Table 3. Cohesive Sediment Data for Degradation Simulation

Set number	Cases number	Inflow discharge (cms)	τ_{cep} (N/m^2)
1	1	100	0.06
	2	200	
	3	400	
	4	800	
2	1	100	0.06
	2		0.4
	3		1.1
	4		3

initial concentration, and numerical parameters of the hypothetical cases for the degradation process are the same as those mentioned in the aggradation process. As shown in Table 3, the present study designs two sets of scenarios in the degradation process including four cases with various inflow discharge and τ_{cep}.

To test the influence of τ_b on bed degradation, four cases of set 1 are designed by changing the inflow discharge. The bed profile simulated by the model shown in Fig. 7(a) indicates that the degradation depth increases gradually from case 1 to case 4. It is clear that the increase of inflow discharge would cause the increase of τ_b, hence, the capability of bed degradation caused by the flow would increase correspondingly. The cases of set 2 are designed to test the influence of τ_{cep} on bed degradation and the simulated results of bed profile are shown in Fig. 7(b). The probability of bed shear stress exceeding τ_{cep} decreases when τ_{cep}
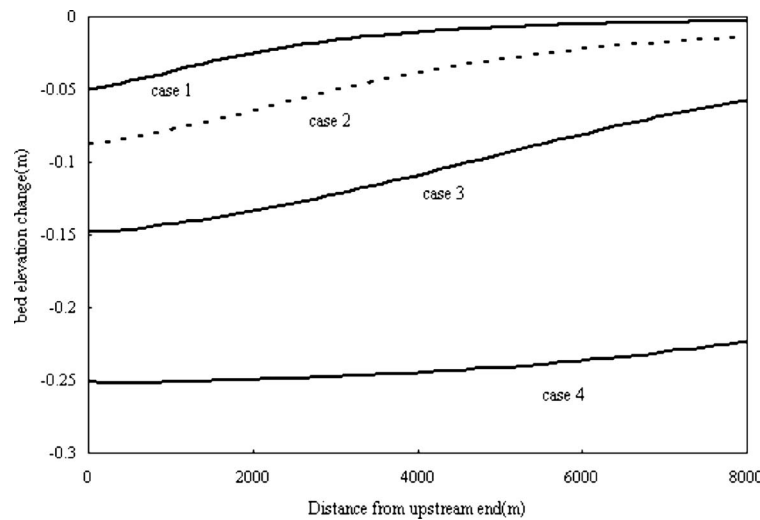
(a) set 1
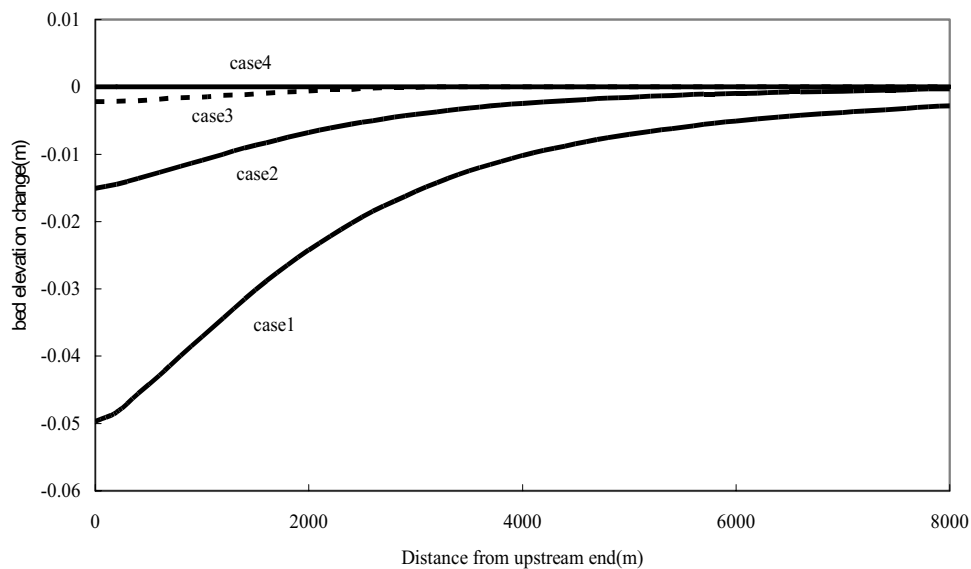
(b) set 2

Fig. 7. Bed elevation change for degradation test of cohesive sediment

Table 4. Cohesive Sediment Data for Consolidation Simulation

Layer number	1 (top)	2	3	4	5	6
Case 1 $\tau_{cep}(N/m^2)$	0.06	0.06	0.06	0.06	0.06	0.06
Case 2 $\tau_{cep}(N/m^2)$	0.06	0.2	1	2	3	3.5

increases, So as shown in Fig. 7(b), the change of bed level caused by degradation process becomes smaller from case 1 to case 4.

Consolidation Process

Two hypothetical cases are adopted to test the function of consolidation processes embedded in the model. The simulated conditions of these two hypothetical cases are the same as the case 1 of set 1 mentioned in the degradation processes. The only difference between two hypothetical cases is the treatment of τ_{cep} in each bed layer. The thickness of each bed layer is set as 1 cm. Case 1 ignores the consolidation effect and each layer specifies the same τ_{cep} value as 0.06 N/m²; in contrast, case 2 takes into account the consolidation effect and each layer specifies different τ_{cep}, as shown in Table 4.

Fig. 8 shows the comparison of bed profile between simulated results for cases 1 and 2. One can observe from Fig. 8 that the maximum degradation depths for cases 1 and 2 are about 5 cm and 1.8 cm, which are located at the fifth and the second layer of initial bed, respectively. It is evident from simulated results that the degradation depth of case 2 is smaller than that of case 1 because the consolidation effect given in case 2 would suppress the bed degradation.

The phenomena interpretation analyzed above indicates a certain extent of acceptability of the model for the simulation of cohesive sediment transport mechanism, although no experiment or field data are available for the validation.
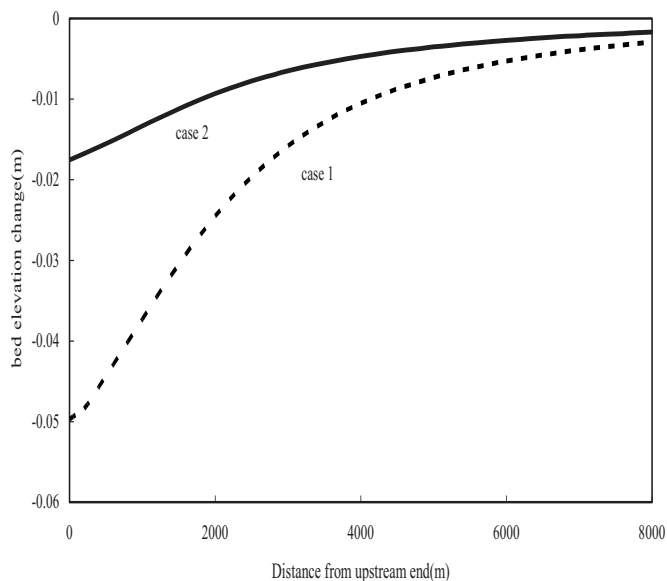

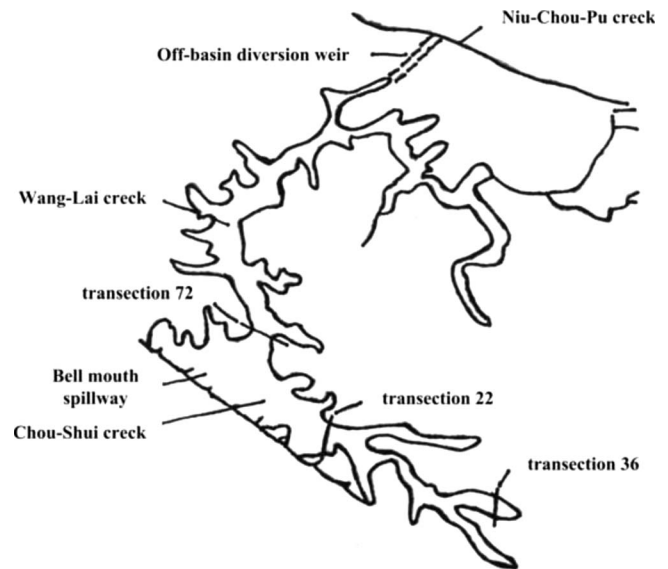**Fig. 8.** Bed elevation change for consolidation cases of cohesive sediment

Fig. 9. Plan layout of Ah Gong Diann Reservoir

Model Application

Study Goal

Ah Gong Diann Reservoir is located at southern part of Taiwan. Due to the loose characteristics of the soil within the catchment, a great amount of soil, in which more than 80% is of cohesive sediment, was carried into the reservoir with the surface runoff. According to the 1991 data, 71% of the storage is occupied by the sediment, which means about 500,000 m³ of sediment was deposited in the storage pond per year. Taiwan Water Resources Agency (WRA) has proposed the "Ah Gong Diann Reservoir Rehabilitation Plan" to improve the capability and life of the reservoir. The rehabilitation plan suggested to lower the inlet of bell mouth spillway down to near the bed level. Instead of flushing the flood, the reconstructed bell mouth inlet will be used to flush the inflow sediment. The layouts of the plan are shown in Figs. 9 and 10. The sluicing gate at the downstream of the tunnel will be opened during the flood season to sluice out the sediment from the reservoir. Moreover, an off-basin diversion weir was constructed to sluice out the flood above the 100-year return period to the Niu-Chou-Pu Creek, located at another catchment near the Ah Gong Diann Reservoir.

Experimental Setup

An experiment (WRA 1999) was conducted to model the sediment flushing efficiency of the Ah Gong Diann Reservoir by following the rehabilitation plan. The layout of the model is shown in Fig. 9. The Chuo-Shui Creek and Wang-Lai Creek inflow boundaries were located at transections 36 and 72, respectively. Based on the rehabilitation plan, the designed channel bed slopes are 4.63×10^{-3} in river portion (from transection 36 to 22) and 1×10^{-3} in reservoir portion (downstream the transection 22), respectively. The sediment dredged from the Ah Gong Diann Reservoir is used for the experiment. In order to obey the dynamic similarity, the Froude number and the ratio of flow velocity and particle fall velocity at rest water, u/w, were used as the controlled dimensionless parameters. To avoid the scale effect, the distorted model, in which the horizontal and vertical scales were
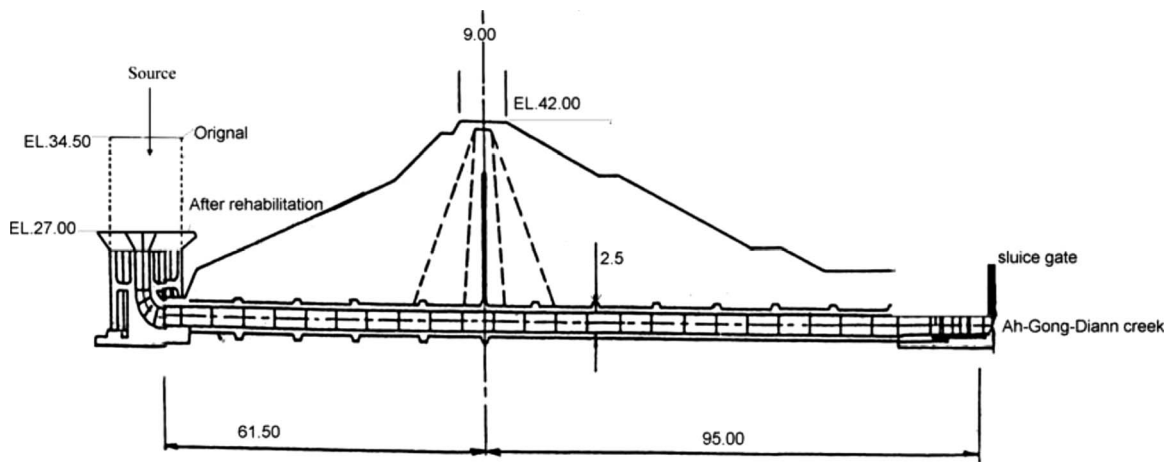
Fig. 10. Cross-sectional layout of rehabilitation plan for bell mouth spillway

1:60 and 1:15, respectively, were used. The velocity ratio and Reynolds number between model and prototype were 1:3.87 and 1:60, respectively.

Treatment of Boundary Conditions

The general layout of the simulation area is shown in Fig. 11, in which the numbers represent the transection locations. There are three types of boundary in this study. Transections 36 and 72 are the Chuo-Shui Creek and Wang-Lai Creek inflow boundaries, respectively; the bell mouth spillway is an outflow boundary; and the other boundaries are solid wall conditions. The treatment of the inflow and solid wall boundaries have been mentioned previously. Flow pattern near the bell mouth spillway in reality is 3D phenomena; obviously, the depth-averaged 2D model is inadequate to explore the bell mouth outflow boundary effect to the flow domain. Nevertheless, for this study the major concern should be the long-term and wide-range evolution processes; the errors induced by the local and short-term effect can be ignored. Hence, the present study set a new outflow boundary, which is the interface section denoted aa′ in Fig. 11, near the bell mouth spillway to substitute the original outflow boundary. By adjusting the water-surface elevation, the outflow rate along the new outflow boundary can be controlled to have the same value as that of the

bell mouth spillway. The new outflow boundary is very close to the bell mouth spillway and the velocity nearby is very small due to the large depth. The influence on the flow and sediment transport phenomenon due to the virtual outflow boundary will be restricted in the local region near the outflow boundary, so the new substitute outflow boundary can be regarded as reasonable for the simulation. The new outflow boundary conditions for experiment and field are the water-surface elevation obtained from measured and reservoir routing, respectively.

Calibration for Numerical Model

The sediment-deposition amount measured along the channel in the experiment will be used to calibrate the parameters in the numerical model. The mesh of 92×14 is used in the simulation. The channel bed slope follows the requirement of rehabilitation plan. Three size classes: 0.172 mm (fine sand, 2.73%), 0.02783 mm (silt, 67.58%), and 0.003873 mm (clay, 29.69%) are chosen to represent the inflow sediment components. The values of τ_{cep} and τ_{cem} are set as 1.1089 N/m^2 (Teisson 1991) to reflect the long-term consolidation effect.

As mentioned previously, the sediment is mainly composed of silt and clay, So the mechanism of deposition for cohesive sediment (i.e., silt and clay) is the key for the model calibration.
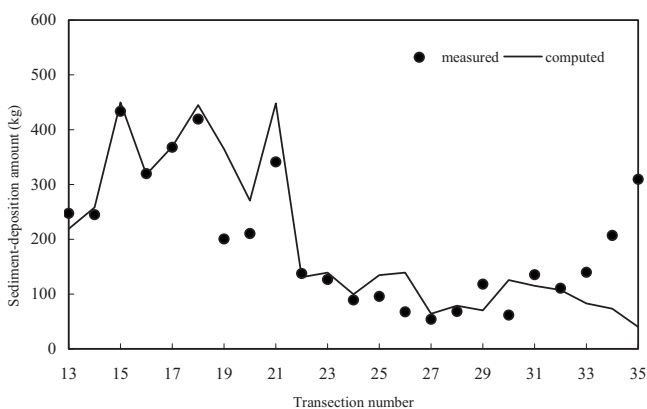

Fig. 11. Plan layout of simulation area

**Table 5.** Regression Coefficients of Total Sediment Load versus τ_{cd} and F

Factor	τ_{cd}	F	R^2
Coefficient	4.53	16.47	99.8%

According to Eq. (10a), the deposition mechanism for cohesive sediment is subject to two factors, including critical shear stress for deposition τ_{cd} and flocculation factor F, which appears in the cohesive sediment fall velocity formula. To investigate the effects of τ_{cd} and F on total sediment-deposition amount (kg) M_s in the Ah Gong Diann Reservoir, a number of test cases are proposed herein for analyses. For each case, there is only one parameter varied while another variable remains fixed. The functional relationship of M_s and τ_{cd} and F in a log-log scale is established as $\ln(M_s) = C_0 + \Sigma_{i=1} C_i \ln(D_i)$ with C_0 being a constant; D_i representing τ_{cd} or F; and C_i being the coefficient associated with D_i. The coefficients obtained by the regression analysis are listed in Table 5. From Table 5, one can observe that F has a more significant effect on M_s than τ_{cd}. Hence, the model is calibrated by adjusting F along the channel and τ_{cd} was set as a fixed value, 0.06 N/m² (Krone 1962).

The 50-year return-period flood case is adopted to calibrate F along the channel. F is adjusted to achieve the best agreement between the simulated results and measured data. The calibrated result is given in Fig. 12, which shows the variation of sediment-deposition amount versus the transection number obtained from simulation and the measured data. One can observe from Fig. 12 that model results generally agree well with measured data except the region near the upstream end. In fact, the excessive deposition near the upstream end is the errors induced by experiments (WRA 1999) due to the difficulty of sediment inflow control. The values of F that yield the best model calibration results almost keep the same in the river portion; in contrast, these values increase from upstream to downstream in the reservoir portion.
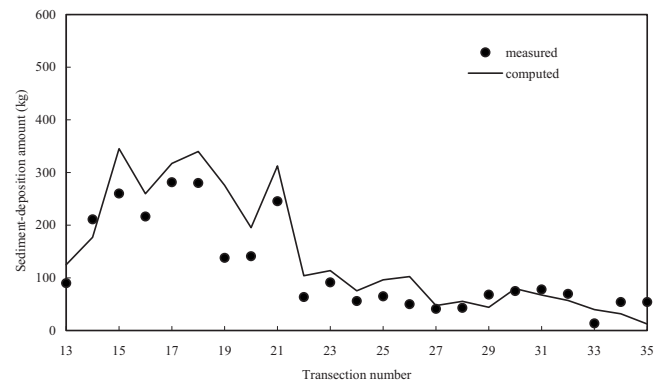
Fig. 13. Variation of sediment-deposition amount versus the transection number for 5-year return period case

The accuracy of the calibrated results is quantitatively assessed by using the data of the 5-year return-period flood case. Fig. 13 shows the corresponding sediment-deposition amount versus the transection number obtained from simulation and the measured data. As shown in Fig. 13, the convincing agreement between the simulated results and measured data is observed. The sediment-deposition amount is relatively small, below 100 kg, in the river portion; in contrast, the sediment-deposition amount becomes larger in the reservoir portion due to the sudden increase of width, water depth, and decrease of velocity.

Efficiency of Sediment Control

After the parameters were validated, the model is applied to predict the sediment-control efficiency of the proposed rehabilitation plan for the real case with various return periods flood. The mesh of 92×14 is used in the simulation.

Table 6 shows the simulated results of efficiency of the sediment control E_i for various return periods, in which E_i can be defined as $E_i = 1 - M_s/M_t$, where M_t represents the total inflow sediment load (kg). It has been found that E_i almost keeps the same, say about 42%, under 50-year return-period flood. Above 100-year return-period, E_i may increase as return period increases. As mentioned before, the off-basin diversion weir becomes effective when the flood exceeds 100-year return period. The flood is diverted and the water-surface elevation near the downstream boundary during the flood may be reduced dramatically. Hence, the influence of the backwater effect may be lower and, as expected, the higher return-period flood should have higher efficiency of sediment control. In summary, the efficiency of sediment control after the rehabilitation plan is completed will reach approximately 56% for 1,000-year return period flood.

Conclusion

An unsteady 2D depth-averaged model for nonuniform sediment transport in alluvial channels has been presented in this paper. In this model, the orthogonal curvilinear coordinate system is

Fig. 12. Variation of sediment-deposition amount versus the transection number for 50-year return period case

Table 6. Simulated Results of Sediment Control Efficiency for Ah Gong Diann Reservoir

Return period (year)	1,000	500	250	200	150	100	50	5	2
E_i (%)	56.23	52.13	48	46.86	45.42	43.81	42.44	42.2	42.46

380 / JOURNAL OF HYDRAULIC ENGINEERING © ASCE / MAY 2009

adopted; the transport mechanisms of cohesive and noncohesive sediment are both embedded; the suspended load and bed load are treated separately. In addition, the computing processes for hydraulic sorting, armoring, and bed consolidation are also included in the model. The model performance has been assessed through the comparison with experimental data and hypothetical test data. The assessment indicates that the model functions well.

The model's applicability has been demonstrated through the application to the Ah Gong Diann Reservoir in Taiwan. Convincing qualitative agreement is achieved between the predicted and observed trends in the sediment-deposition amount change for both the parameter calibration and validation processes. The efficiency of sediment control for the reservoir is numerically determined by using the proposed model.

Acknowledgments

Notation

The following symbols are used in this paper:

C = concentration;
C_d = near-bed deposition concentration;
C_e = entrainment near-bed concentration;
C_F = coefficient;
C_f = friction factor;
C_0 = constant;
c = Chezy factor;
c_1 = grain Chezy coefficient;
D = sediment diameter;
D_i = representing τ_{cd} or F;
D_m = smallest nonmoving size class;
D_{50} = median sediment-particle size;
D_{*k} = dimensionless particle diameter;
d = water depth;
E = roughness parameter;
E_i = efficiency of the sediment control;
E_m = active-layer thickness;
e_η = lateral dispersion coefficient;
F = flocculation factor;
F_d = characteristic depth of erosion;
g = gravitational acceleration;
h_1 and h_2 = metric coefficients in ξ and η directions, respectively;
M = material coefficient;
M_s = total sediment-deposition amount;
p = porosity of the bed material;
Q_1, Q_2 = suspended-sediment flux due to both turbulent diffusion and lateral dispersion in the ξ and η directions, respectively;

q_{b_1}, q_{b_2} = components of bed-load flux in the ξ and η directions, respectively;
$q_{b_i}^t$ = theoretical bed-load transport capacity in the i (ξ or η) direction;
r = radius of curvature;
S = suspended-sediment source;
S_d = deposition component;
S_e = entrainment component;
S_f = active-layer floor source;
s = dimensionless sediment density;
$T_{i,j}$ = integrated effective stress;
T_k = transport-stage parameter;
t = time;
U_* = shear velocity;
u = ξ components of velocity;
u_w = depth-averaged velocity near the wall;
u_* = effective bed-shear velocity;
u_{*c} = critical shear velocity evaluated from Shields diagram;
v = η components of velocity;
w_s = particle settling velocity following the Stokes law;
w_l = lift-off velocity;
w_f = sediment fall velocity;
y_w = distance between the first computational grid point adjacent to the wall and the wall itself;
z_b = bed elevation;
z_s = water surface elevation;
β = active-layer size fraction;
β_s = active stratum size fraction;
Δt = time step;
ε_ξ and ε_η = turbulent diffusion coefficients in the ξ and η directions, respectively;
ζ = hiding factor;
ξ and η = orthogonal curvilinear coordinates in streamwise axis and transverse axis, respectively;
ρ = fluid density;
ρ_d = bulk density;
ρ_s = density of sediment;
τ_{b1}, τ_{b2} = ith direction components of free-surface and bed-shear stress, respectively;
τ_{cd} = critical shear stress for deposition;
τ_{cem} = critical bed shear stress for mass erosion; and
τ_{cep} = critical shear stress for particle erosion.

Superscripts

n = variables at time level n;
$n+1$ = variables at time level $(n+1)\Delta t$; and
$\overline{(\ )}$ = depth average.

Subscripts

b = dependent variables at channel bed;
k = kth size class; and
s = dependent variables at the water surface.

References

Almquist, C. W., and Holley, E. R. (1985). "Transverse mixing in meandering laboratory channels rectangular and naturally varying cross-section." *Technical Rep. No. 205*, Center for Research in Water Resources, Univ. of Texas at Austin, Austin, Tex.

Ariathurai, R. (1974). "A finite element model for sediment transport in estuaries." Ph.D. thesis, Dept. of Civil Engineering, Univ. of California, Davis, Calif.

Bennett, J. P., and Nordin, C. F. (1977). "Simulation of sediment transport and armoring." *Hydrol. Sci. Bull.*, 37, 2119–2162.

Biglari, B., and Sturm, T. W. (1998). "Numerical modeling of flow around bridge abutments in compound channel." *J. Hydraul. Eng.*, 124(2), 156–164.

Borah, D. K., Alonso, C. V., and Prasad, S. H. (1982). "Routing graded sediments in streams: Formulations." *J. Hydr. Div.*, 108(12), 1486–1505.

Celik, I., and Rodi, W. (1988). "Modeling suspended sediment transport in nonequilibrium situations." *J. Hydraul. Eng.*, 114(10), 1157–1191.

Elder, J. W. (1959). "The dispersion of marked fluid in turbulent shear flow." *J. Fluid Mech.*, 5(4), 544–560.

Fang, H. W., and Wang, G. Q. (2000). "Three-dimensional mathematical model of suspended-sediment transport." *J. Hydraul. Eng.*, 126(8), 578–592.

Fischer, H. B., List, E. J., Koh, R. C. Y., Imberger, J., and Brookes, N. H. (1979). *Mixing in inland and coastal waters*, Academic, San Diego.

Holly, F. M., and Rahuel, J. L. (1990). "New numerical physical framework for mobile-bed modeling." *J. Hydraul. Res.*, 28(4), 401–416.

Hsieh, T. Y., and Yang, J. C. (2003). "Investigation on the suitability of 2D depth—Averaged models for bend-flow simulation." *J. Hydraul. Eng.*, 129(8), 597–612.

Hsieh, T. Y., and Yang, J. C. (2004). "Implicit two-step split-operator approach for modelling two-dimensional open channel flow." *J. Hydrosci. Hydr. Eng.*, 22(2), 113–139.

Hsieh, T. Y., and Yang, J. C. (2005). "Numerical examination on the secondary-current effect for contaminant transport in curved channel." *J. Hydraul. Res.*, 43(6), 643–658.

Hu, C., and Hui, Y. (1996). "Bed-load transport. I: Mechanical characteristics." *J. Hydraul. Eng.*, 122(5), 245–254.

Karim, M. F., Holly, F. M., and Yang, J. C. (1987). "IALLUVIAL: Numerical simulation of mobile-bed rivers. Part I. Theoretical and numerical principles." *Rep. No. 309*, Iowa Institute of Hydraulic Research, Univ. of Iowa, Iowa City, Iowa.

Kassem, A. A., and Chaudhry, M. H. (2002). "Numerical modeling of bed evolution in channel bends." *J. Hydraul. Eng.*, 128(5), 507–514.

Krone, R. B. (1962) "Flume studies of the transport of sediment in estuarine shoaling processes." *Technical Rep.*, Hydraulic Engineering Lab., Univ. of California, Berkeley.

Lane, E. W., et al. (1974). "Report of the subcommittee on sediment terminology." *EOS Trans. Am. Geophys. Union*, 128(6), 936–938.

Li, C. W., and Ma, F. X. (2001). "3D numerical simulation of deposition patterns due to sand disposal in flowing water." *J. Hydraul. Eng.*, 127(3), 209–218.

Lin, B. (1984). "Current study of unsteady transport of sediment in China." *Proc., Japan-China Bi-Lateral Seminar on River Hydraulics and Engineering Experiences*, 337–342.

Migniot, C. (1989). "Bedding-down and rheology of muds. Part I." *Houille Blanche*, 1, 11–29 (in French).

Partheniades, E. (1965). "Erosion and deposition of cohesive soils." *J. Hydr. Div.*, 91(1), 105–139.

Rastogi, A. K., and Rodi, W. (1978). "Prediction of heat and mass transfer in open channels." *J. Hydr. Div.*, 104(3), 397–420.

Rijn, L. C., Rossum, H., and Termes, P. (1990). "Field verification of 2-D and 3-D suspended-sediment models." *J. Hydraul. Eng.*, 116(10), 1270–1288.

Shimizu, Y., and Itakura, T. (1989). "Calculation of bed variation in alluvial channels." *J. Hydraul. Eng.*, 115(3), 367–384.

Spasojevic, M., and Holly, F. M. (1990). "2-D bed evolution in natural watercourses—New simulation approach." *J. Waterway, Port, Coastal, Ocean Eng.*, 116(4), 425–443.

Struiksma, N. (1985). "Prediction of 2D bed topography in rivers." *J. Hydraul. Eng.*, 111(8), 1169–1182.

Suryanarayana, B. (1969). "Mechanics of degradation and aggradation in a laboratory flume." *Engrg. hydr.*, Colorado State Univ., Fort Collins, Colo.

Teisson, C. (1991). "Cohesive suspended sediment transport: Feasibility and limitations of numerical modeling." *J. Hydraul. Res.*, 29(6), 755–769.

Thomas, W. A., and McAnally, W. H. (1985). *User's manual for the generalized computer program system open-channel flow and sedimentation TABS-2*, Dept. of the Army Waterways Experiment Station, Corps of Engineers, Vicksburg, Miss.

Van Rijn, L. C. (1984a). "Sediment transports. Part I: Bed load transport." *J. Hydraul. Eng.*, 110(10), 1431–1456.

Van Rijn, L. C. (1984b). "Sediment transports. Part II: Suspended load transport." *J. Hydraul. Eng.*, 110(11), 1613–1641.

WRA. (1999). "Hydraulic model study of the desilting functions of sluiceway in Ah Gong Diann Reservoir." *Technical Rep.*, Water Resources Planning Institute, Water Resources Agency, Ministry of Economic Affairs, Taiwan, R.O.C. (in Chinese).

Wu, W., Rodi, W., and Wenka, T. (2000). "3D numerical modeling of flow and sediment transport in open channels." *J. Hydraul. Eng.*, 126(1), 4–15.

Ziegler, C. K., and Nisbet, B. S. (1995). "Long-term simulation of fine-grained sediment transport in large reservoir." *J. Hydraul. Eng.*, 121(11), 773–781.